



Relationship between material pitting and cavitation field impulsive pressures



Jin-Keun Choi*, Georges L. Chahine

DYNAFLOW, Inc., 10621-J Iron Bridge Road, Jessup, MD, USA

ARTICLE INFO

Article history:

Received 7 October 2015

Received in revised form

16 January 2016

Accepted 20 January 2016

Available online 4 February 2016

Keywords:

Cavitation erosion

Erosion modeling

Cavitation pit

Bubble dynamics

Fluid structure interaction

ABSTRACT

Material pitting from cavitation has been used on and off as an indicator of the vague concept of 'cavitation intensity'. Periodically, some researchers suggest the use of pitting tests as a means to provide quantitative measurements of the amplitude of the impulsive pressures in the cavitation field, especially when combined with Tabor's formula or with finite element computations with idealized synthetic loads. This paper examines the viability of such a suggested method using fully coupled bubble dynamics and material response, and strongly concludes that the method provides at best a qualitative assessment of the cavitation erosion potential. Peak pressures deduced from pit geometry are significantly lower than the ones actually applied. In addition the correspondence is highly dependent on the way the load is applied and different loading scenarios with the same amplitude of the cavitation impulsive pressure result in different pit aspect ratios.

© 2016 Elsevier B.V. All rights reserved.

1. Introduction

A material surface, which is exposed to cavitation, progressively erodes over time due to local high amplitude short duration and small footprint loads from repeated individual and collective cavitation bubble collapse [1]. Proper modeling of the physical phenomena at play is complex and requires understanding and description of both the two-phase fluid flow and the material dynamics as well as their interaction. Cavitation initiates from bubble nuclei in the liquid, which when exposed to low pressures grow explosively then collapse violently when the pressure recovers, thus generating very high local pressures and shock waves [1–4]. When a bubble collapses onto a material surface, a reentrant micro jet forms in the largely deformed bubble, vectors towards the material and impacts its surface with shock waves forming in the subsequent dynamics [5–9]. The flow due to the bubble collapse and the reentrant jet impact generate high impulsive stress into the material. When these exceeds the elastic limit of the material, permanent deformation occurs and a microscopic pit is generated [10]. This initial phase of material response to the cavitation field, the “incubation period”, does not involve any mass loss. With repeated impacts, hardening of the

material surface layer develops, which could be used for material peening [11,12], then pits accumulate and finally micro-failures occur resulting in material removal and weight loss.

In order to characterize cavitation erosion for different cavitation conditions (e.g. different flow field velocities, or comparison between small scale laboratory accelerated erosion tests and full scale conditions), a well-defined method to characterize the intensity of the cavitation flow field at the exposed material surface is needed. Pressure transducers are the obvious first choice, but they have limitations due to their size, which is often much larger than the cavitation bubbles, and their resonance frequency, which is often lower than the required high frequency pressures generated by the small microbubbles [1,13]. Another method, which has been periodically proposed during the past century, is to conduct pitting tests. In this case, short duration cavitation tests are conducted within the incubation period where non-overlapping pits are produced. These pits are then measured and characterized to deduce from their distribution and geometry the hydrodynamic flow field pressures (e.g. [3,14–16]). Cavitation pitting studies dates back to the early 1900's when Parsons and Cook [17] observed the depth and dimensions of the pitted areas on marine propellers. Since then, many researchers have tried to correlate the location of pitting with cavitation bubble clouds along with statistics of pit number and pit diameters and depths [2,18–24]. More recently, pitting tests were also conducted using thin copper foil in order to capture relatively small magnitude impacts [25]. With the advances in modern imaging and micro-measurement techniques, recent studies reveal

* Corresponding author.

E-mail address: jkchoi@dynaflow-inc.com (J.-K. Choi).

URLS: <http://www.dynaflow-inc.com> (J.-K. Choi),

<http://www.dynaflow-inc.com> (G.L. Chahine).

more details of the pit shapes and pit statistics [1,26]. All these studies, however, did not use or provide direct quantitative relationships between the cavitation field pressures and the generated pits.

More recently, there have been renewed effort to correlate the cavitation field impulsive pressure and the measured pits characteristics [7,27,28], in which attempts have been made to correlate the experimentally measured ratios of pit depth to diameter to the pressure field using the spherical indentation relationships developed by Tabor [29] and making, without real justification, the major assumption that spherical indentations (rigid load/material interface and strain rates, $\sim 0.05 \text{ s}^{-1}$) and collapsing bubbles (deforming liquid/material interface and strain rates, $\sim 10^4 \text{ s}^{-1}$) produce similar loads on the material. An effort to include the strain rate dependency of the stress–strain curves was attempted in [28] but static loads only were still considered. Recently, finite element method analysis was also conducted [30–31] using the same basis for the load as in the Tabor approach, i.e. time independent idealized constant pressure load, and obviously, due to the over-simplified parameters, an almost one-to-one relationship between the loads and the pit geometry characteristics was found. The time dependent analysis in [32] confirmed that such one-to-one relation is achieved only when the time scale of the load is larger than $10^5 \mu\text{s}$ (see Fig. 5 of [32]), which is huge compared to the duration of bubble dynamics generated peak pressures.

The believers in the pitting technique claim that the method allows the material to be used as a high fidelity recorder of the cavitating field pressures and that the results would be independent of the material used [16,27,31]. Actually, a first strong limitation of this statement is that only pressures that lead to stresses higher than the elastic limit of each particular material will form pits and all lower pressures cannot be measured. Thus, each material acts as a high pass filter and records only the pressures above a cutoff value, which is material dependent. Other even more significant limitations are examined in more details in this paper using advanced bubble dynamics–material dynamics interaction modeling techniques [7,8,33] and stem from the examination of the quantitative relationship between pit characteristics and actual dynamic pressure loads.

In order to investigate this relationship, a numerical fluid–material interaction approach is undertaken to investigate pitting formation from the combined bubble dynamics and material mechanics viewpoints. Fully coupled Fluid Structure Interaction (FSI) simulations are conducted and provide both the actual liquid generated pressures and the resulting material pit characteristics. Using these results, the actual pressure applied on the material surface is compared with the one deduced from the pit geometry using the Tabor equations [29]. The same approach is also applied using synthetic loads (prescribed loading, no FSI) as published in previous work [30–33] where the applied load is specified and the resulting material pits deduced and the results compared to the Tabor predictions.

2. Material/Fluid interaction simulations

In this study, correlation between the cavitation pressures in the liquid and the resulting pit characteristics is studied using FSI coupled material finite element method simulations with fluid dynamic simulations of bubble collapse of various intensities. We describe briefly below the methods used and refer the reader to much detailed descriptions in Refs. [7–9] as well as other references cited below.

2.1. Bubble dynamics

The numerical approach applied to model material pitting is part of a general hybrid FSI approach we developed to simulate fluid structure interaction problems involving shock and bubble dynamics encountered in cavitation and underwater explosion bubbles [34–37]. During a major portion of the bubble growth and collapse history, the velocities in the liquid are much smaller than the liquid speed of sound, and an incompressible approach is justified. A potential flow boundary element code, 3DYNAFS-BEM[®] [34,35,38] is used during this time period. On the other hand, shock waves and strong compressibility of the liquid come into play during the last stage of the bubble collapse and following reentrant jet impact on the material. A time decomposition approach is then used to switch for the incompressible solution to fully compressible solvers such as GEMINI [36] or 3DYNAFS-COMP[®] [39]. This time decomposition hybrid procedure combining incompressible and compressible solvers to capture the full dynamics has been described in details in [37]. The procedure takes advantage of the capabilities of 3DYNAFS-BEM[®], to produce very accurate capturing of the reentrant jet [40], and GEMINI and 3DYNAFS-COMP[®], which have been proven very good at capturing shock dynamics and resulting pressures on the boundaries [41]. Description of both methods and the coupling procedure can be found in [35,39]. Illustrations of the results are shown later below.

2.2. Material response

The dynamics of the material is modeled by the finite element model DYNA3D, which is a non-linear explicit structure dynamics code developed by the Lawrence Livermore National Laboratory [42]. The US Navy version used in this paper is named DYNA. The structural code computes the material deformation with the loading being provided here by the fluid solution (either 3DYNAFS-BEM[®], 3DYNAFS-COMP[®], or GEMINI). DYNA uses a lumped mass formulation for efficiency. This produces a diagonal mass matrix \mathbf{M} , to express the dynamics equation as:

$$\mathbf{M} \frac{d^2 \mathbf{x}}{dt^2} = \mathbf{F}_{\text{ext}} - \mathbf{F}_{\text{int}}, \quad (1)$$

where \mathbf{F}_{ext} represents the applied external forces, and \mathbf{F}_{int} the internal forces. The acceleration, $d\mathbf{x}^2/dt^2$, for each element is obtained through an explicit temporal central difference method. Additional details on the general formulation can be found in [42].

2.3. Cavitation and material interactions

Material–fluid interaction effects are captured in the simulations by coupling at each computation time step the fluid codes and DYNA3D using a coupler interface. The step-by-step coupling is achieved by following the numerical procedure below:

Step 1: The relevant fluid code computes the pressures at all material surface nodes.

Step 2: In response to this pressure loading, the material code computes material deformations, stresses, strains, and the surface node velocities.

Step 3: The coordinates and the velocities of the material surface nodes then define new boundary conditions for the fluid code at the following time step.

Step 4: The relevant fluid code then solves the flow field using the material surface node positions and normal velocities and deduces the liquid pressures at the material surface for the next time step, looping back to **Step 2**.

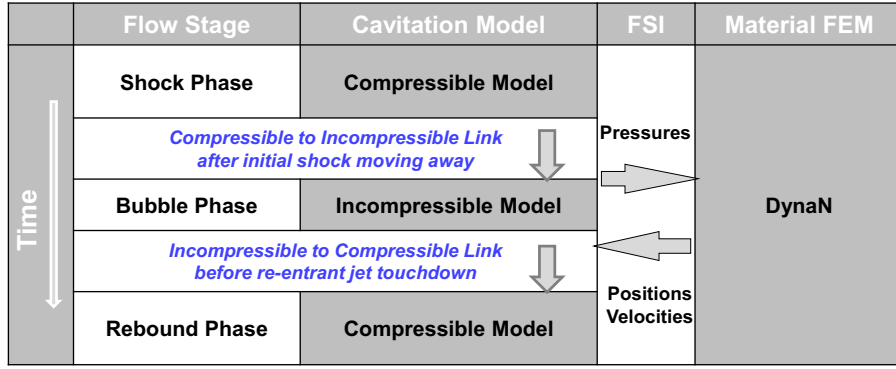


Fig. 1. Schematic diagram of the numerical approach used to simulate the interaction between a cavitation bubble and a material surface.

This procedure is illustrated in Fig. 1. Additional details on the methods described above can be found in [37].

2.4. Synthetic loading

Another procedure to examine the validity of the Tabor equation approach is for us to use the finite element method described above and provide input excitation synthetically using an analytical representation, which corresponds to measured typical cavitation events pressure signals [13,43]. Compared to fully coupled simulations, where it is rather lengthy to vary the impact pressure magnitude and duration systematically, synthetic loading enables one to study more easily the effects of systematic variations of the magnitude, duration, and spatial extent of the impact loads. Previous numerical and experimental studies indicate that the pressure peaks in the cavitation fields can be represented well with a Gaussian function varying both in space and time for both ultrasonic and hydrodynamic cavitation conditions [13]. This representation (usually with the simplification of ignoring the time dependency) has been also adopted by other researchers in the field [13,30,31].

Thus, in this paper, we consider simulations where, in addition to the actual computed bubble collapse pressures, idealized time and space varying impact pressure loadings, $P(r,t)$, in the following form are imposed:

$$P(r,t) = P_0 e^{-\left(\frac{t}{\Delta t}\right)^2} e^{-\left(\frac{r}{\Delta r}\right)^2}, \quad (2)$$

where P_0 is the amplitude of the pressure pulse, Δt is its characteristic duration, and Δr is its footprint characteristic radius.

2.5. Materials considered

In this study of the correlation between liquid pressures loading the material and pit characteristics, four metals (Aluminum 1100, Aluminum 7075, Nickel Aluminum Bronze, and Stainless Steel A2205) are considered. These metals were modeled using elastic–plastic models with linear slopes (constant moduli), one for the initial elastic regime and the second, a tangent modulus, for the plastic regime as shown in Fig. 2. The corresponding material parameters are shown in Table 1. A more complete model, which includes strain rate effects, the Johnson–Cook model [44], has also been used but the results are not shown here to simplify the presentation and illustrate the issues with using pitting results to deduce the loads.

3. Deducing loads from Tabor equation

In Tabor's approach [29], a spherical indentation characterized by its diameter D and depth h as illustrated in Fig. 3 is considered.

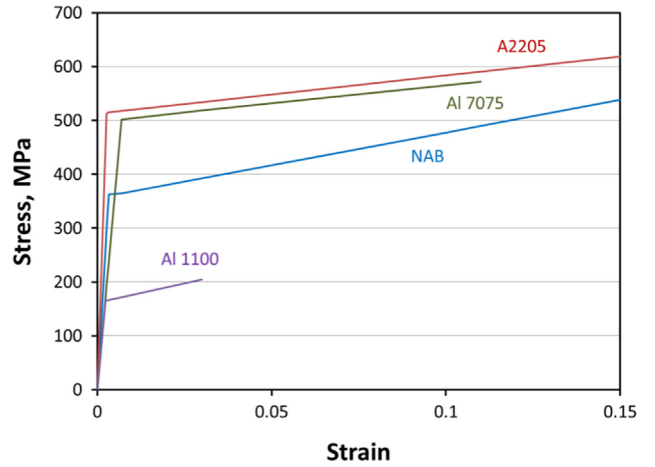


Fig. 2. Simple assumed elastic–plastic stress–strain relations of the four materials investigated in this study.

Table 1
Properties of the material investigated in this study.

Metallic material	Yield stress (MPa)	Young's modulus (GPa)	Tangent modulus (MPa)	Elongation at break	Density (g/cm^3)
Al 1100	165	69	1449	0.03	2.71
NAB	360	110	1216	0.25	7.64
Al 7075	503	71.7	670	0.11	2.81
SS A2205	515	190	705	0.35	7.88

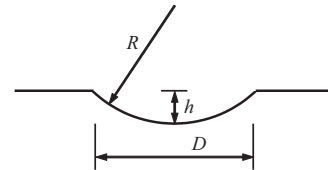


Fig. 3. Sketch showing an idealized cavitation pit considered as a spherical pit.

The mean strain, ϵ_m , resulting from forming the pit in the material is estimated by:

$$\epsilon_m = k \frac{D}{2R}, \quad (3)$$

where R is the radius of the sphere that fits the spherical indent and k is a coefficient close to 0.2 [28]. From geometrical relations of the spherical shape, Eq. (3) can be re-written as:

$$\epsilon_m = 0.8 \frac{h/D}{1 + 4(h/D)^2} = 0.8 \frac{\xi}{1 + 4\xi^2} \quad \text{with } \epsilon = h/D. \quad (4)$$

This equation shows that the mean strain associated with a spherical pit is related to the geometric aspect ratio, ξ , which is usually measured experimentally to represent the material deformation factor from pitting data and deduce the corresponding load [27,28].

The corresponding maximum strain is then deduced from this mean strain assuming an exponential strain distribution of exponent, θ , in the depth direction [27]:

$$\epsilon_{max} = \epsilon_m(1 + \theta). \quad (5)$$

The users of this method report that can be obtained experimentally and give values for the materials used in this study [7,27].

From the maximum strain, the corresponding maximum stress can be deduced using the stress–strain relations of the material. In this approach, the maximum stress is assumed to occur at the surface of the material, and for the proponents of using pitting to measure liquid pressures, this stress is equated to the peak of the impulsive cavitation field pressure at the material surface.

4. Material loading

4.1. Pressure driving bubble collapse

It is known that microbubbles or nuclei are omnipresent in liquids and, once excited by local pressures decreasing below a critical value (a commonly used value is the liquid vapor pressure), they grow explosively until their internal pressure drops below the liquid local pressure [3,4,45]. The bubbles then collapse violently, producing intense pressures, emitting sound, and eroding any solid surfaces in their proximity. To simulate a bubble dynamics pressure field under such a condition, we consider a nucleus initially at equilibrium with the surrounding liquid and we subject it to a time dependent pressure field, which would correspond to what the bubble would see while moving in the flow close to the material surface. We impose first a pressure drop to a value below the bubble critical pressure, keep this pressure for a prescribed time, Δt , then increase it to a high value, which is kept until the end of the computation.

Fig. 4 illustrates this for the case of a bubble of initial radius $R_0=50 \mu\text{m}$ at equilibrium in the liquid at 1 atm (10^5 Pa). The pressure is then suddenly decreased to 10^3 Pa , and kept there for

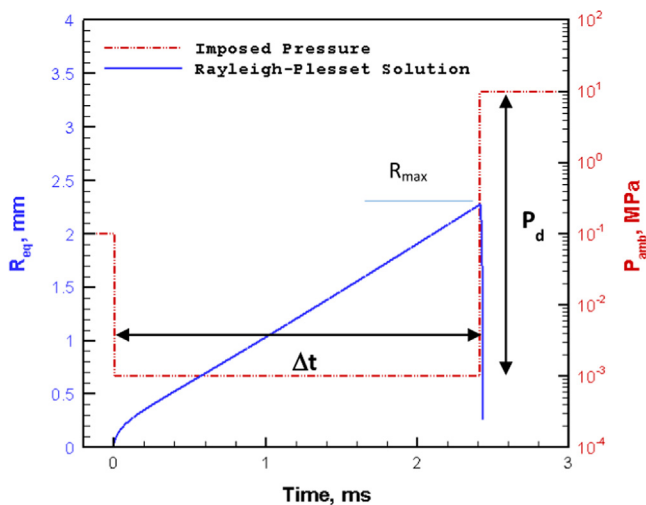


Fig. 4. Imposed time dependent pressure field (red dashed curve) around a spherical bubble of $50 \mu\text{m}$ initial radius and resulting bubble radius vs. time (blue solid curve) as predicted by the solution of the Rayleigh–Plesset equation. (For interpretation of the references to color in this figure legend, the reader is referred to the web version of this article.)

$\Delta t=2.415 \text{ ms}$, and then is increased sharply to $P_d=10 \text{ MPa}$. Fig. 4 also shows the response of a spherical bubble to this pressure function (in reality, the bubble will strongly deform as we will see below but this illustrates roughly the bubble volume change) obtained by integrating the Rayleigh–Plesset equation. It is seen that, as soon as the ambient pressure drops to the low value (10^3 Pa), the bubble responds and starts growing. The bubble cannot reach an equilibrium size and continues to grow during Δt until the sudden pressure increase to P_d occurs. A maximum bubble size, R_{max} , is reached shortly after the overpressure is imposed due to liquid inertia. This is followed by a strong collapse of the bubble. (Fig. 5).

In this study, fully coupled FSI simulations were conducted with the magnitude of the collapse driving pressure, P_d , varying between 0.1 MPa and 20 MPa. The duration of the pressure drop was varied such that the achieved bubble maximum radius, R_{max} achieved the sizes 0.5, 1.0, 1.5 and 2.0 mm. The bubble standoff, X , from the nearby material surface was also varied to correspond to 0.5, 0.75, 1.0, and 1.5 R_{max} .

4.2. Numerical discretization

The FSI simulations were conducted during the bubble collapse phase when the stresses caused material response or deformation. For the liquid bubble dynamics simulations an axisymmetric domain with a total of 220×1470 grid points was used with a stretched grid to cover a $1 \text{ m} \times 1 \text{ m}$ physical domain. The mesh spacing was distributed such that there was a uniform fine mesh with a size of $10 \mu\text{m}$ covering the bubble/material area of interest where the interaction between bubble and material is important. The axisymmetric half-infinite computational domain was bounded by the material surface and far field grids away from the bubble. Transmission non-reflective boundary conditions, i.e. the flow variables are extrapolated along the characteristic wave direction, were imposed at the far field boundaries. On the axis of symmetry all physical variables such as density, pressure, velocity, and energy have zero gradients.

For the material dynamics computations, axisymmetry was also used, and the material was supposed to be in a circular plate with a radius of 1 m and a thickness of 0.01 m with discretized rectangular brick elements. As shown in Fig. 6, a stretched grid with 220 elements in the radial direction, r , and 446 elements in the axial direction, z , were used to discretize the plate. Near the center of the plate ($r=0$) where the high pressure loading occurs, fine elements of $10 \mu\text{m}$ size were used. The motion of the nodes at the plate bottom was restricted in all directions. On the axis of symmetry the nodes were allowed to move only in the vertical direction.

4.3. Synthetic loading

Synthetic loading as described in Section 2.4 was also considered to investigate the resulting material response. Typical load ranges based on previous numerical and experimental studies of cavitation erosion [7,8,13,26] were used. These were as follows: pressure load amplitudes between 1 MPa and 2 GPa, load durations between 0.1 μs and 2 μs , and load radial extents (spatial footprints) between $10 \mu\text{m}$ and $100 \mu\text{m}$. An illustration of the Gaussian load varying in time with peak at $t=2.5 \mu\text{s}$ is shown in Fig. 7. Only one parameter of the synthetic load was varied at a time to produce one loading condition shown in the data below. Early results of this approach were presented in [33].

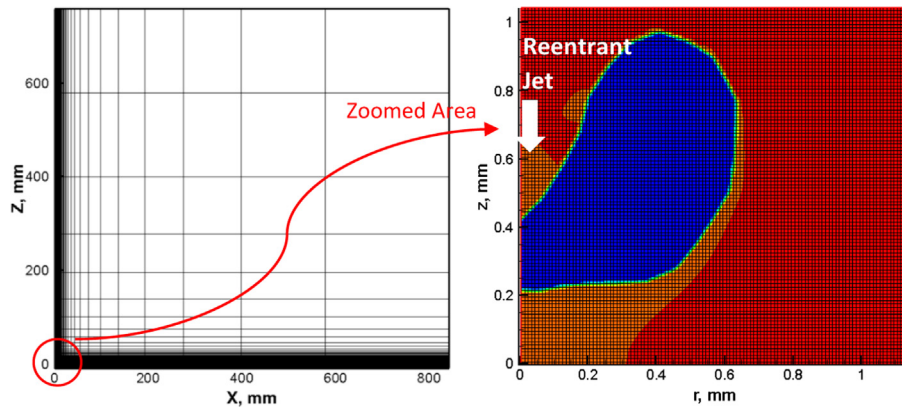


Fig. 5. Axisymmetric fluid computational domain used for the computation of the bubble dynamics: full domain (right), zoomed area at the bubble location (left). The purple region is the inside of the deformed bubble with a well-developed reentrant jet at the axis of symmetry.

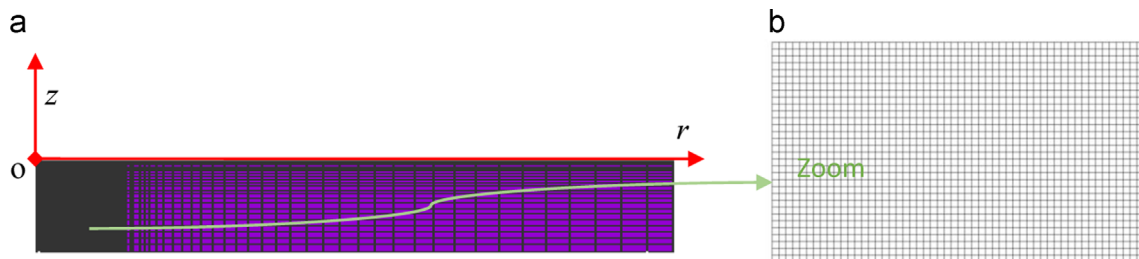


Fig. 6. Finite element axisymmetric grid used in DYNA3D to study the material response to loads due to collapsing cavitation bubbles. (a) Coordinate system with stretched grid at far field, and (b) zoom near (0,0) showing uniform mesh with 10 μm spacing.

5. Results and discussion

5.1. FSI simulations of pit formation and pit geometry

In order to examine the validity of inferring from the pit geometrical shape factor, ξ , the magnitude of the impulsive pressure generated by cavitation bubble collapse, we conducted an extensive series of CFD and material finite element (FEM) simulations of pit formation in a material exposed to two types of loads:

- fully coupled fluid structure interaction (FSI) simulations of bubble dynamics and material response;
- material deformation due to synthetic loading configurations where we varied systematically the amplitude, space extent, and duration of the load.

The FSI simulations briefly described above modeled bubble shape deformation, reentrant jet development, compressible impact of the jet on the material with generation of a water hammer impact and emission of a shock wave. Bubble size, standoff from wall, and collapse driving pressure functions were varied to cover a range of FSI conditions.

Figs. 8–10 illustrate some details of the bubble dynamics and interaction with the nearby material. This particular bubble dynamics and material conditions shown in the figures correspond to bubble of initial radius $R_0=50\ \mu\text{m}$, maximum radius $R_{max}=2\ \text{mm}$, at a standoff distance of $d_0=1.5\ \text{mm}$ from the material, while the collapse driving pressure was $P_d=10\ \text{MPa}$. Fig. 8 shows bubble shape outlines at different instants during the bubble collapse. These shapes were obtained from the boundary element method solution and clearly show the development of the reentrant jet and its fast motion towards the opposite side bubble before striking the material boundary. Jet speed, jet geometric characteristics and momentum all are provided by the solution as described in [7,8,9]. Fig. 9 shows bubble shapes and pressure contours obtained with the compressible flow solution [39]. Very high pressures can be seen and are generated by liquid–liquid

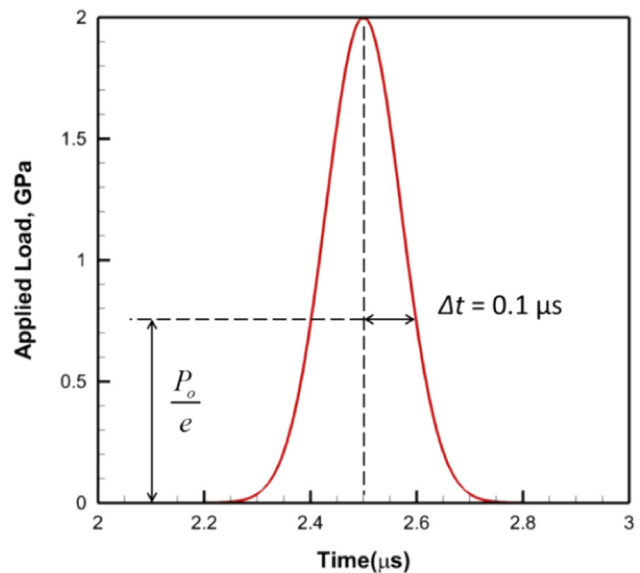


Fig. 7. Illustration of the Gaussian load varying in time. Peak pressure 2 GPa, $\Delta t=0.1\ \mu\text{s}$.

impact at the time of reentrant jet impact on the opposite side of the bubble ($t\sim 0.05\ \mu\text{s}$) and at the time of the jet–material wall impact ($t\sim 0.4\ \mu\text{s}$). Fig. 10 illustrates the pressures generated at the center of the material liquid interface at the material origin of coordinates. The liquid–liquid impact event generates a localized high pressure region which expands quasi spherically to the wetted material surface (first pressure peak in Fig. 10). The bubble ring left after the jet touchdown, shrinks then collapses generating another high pressure wave (second peak in Fig. 10). Extensive details of this physics is described in [7,8,9]. The material responds by developing an indentation corresponding in time to the high

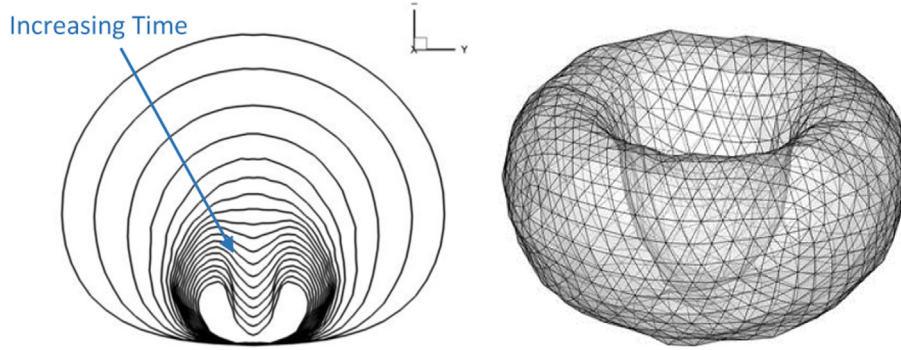


Fig. 8. Bubble cross-section shape evolution in time during bubble collapse near the material wall (left), and 3D view of an instant prior to reentrant jet touchdown on the opposite side of the bubble (right).

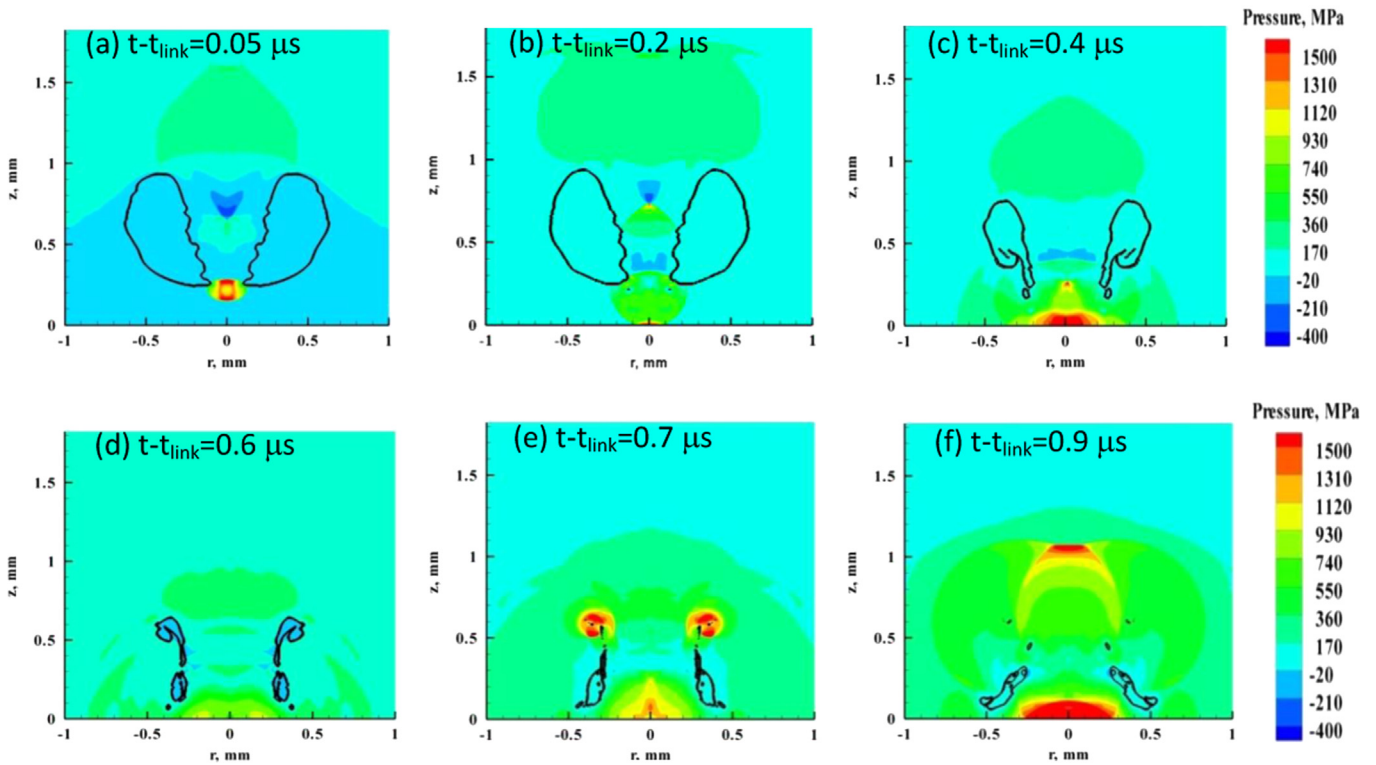


Fig. 9. Example bubble shapes and pressure field during bubble collapse near a wall [8]. Initial bubble radius $R_0=50 \mu m$, $R_{max}=2 mm$, $d_0=1.5 mm$, the initial standoff $\bar{X}=0.75$, and collapse driving pressure $P_d=10 MPa$ [8].

pressure generation as illustrated in Fig. 10. Due to the high pressure generated by the collapse, the material deforms elastically first, then exceeds the elastic limit resulting in unrecoverable plastic deformation and a pit, in this case of a depth of about $10 \mu m$. The ensuing oscillations in the material deformation take a few tens of microseconds.

5.1.1. Stress and strain in the material

To understand the material response, stress and strain distributions inside the material are examined in Figs. 11 and 12. Here we consider an example of synthetic loading with duration $\Delta t = 0.1 \mu s$ and spatial radial extent, $\Delta r = 100 \mu m$. The amplitude of the selected impact is $P_0=2 GPa$ and the material is Stainless Steel A2205. Fig. 11 (left) shows contours of the effective stress distribution, or von Mises stress, $\sigma_v = \sqrt{(3/2)s_{ij}s_{ij}}$, where s_{ij} is the deviatoric stress tensor under the impacted surface when the maximum deformation of the material surface center is reached

($t=2.5 \mu s$). The highest stresses are observed below the material surface at a depth of the same order as the load radial extent, Δr . This is a first important difference with the Tabor method assumptions.

Fig. 11 (right) shows at the same time instant the distribution of the effective plastic strain defined as $\epsilon_v = \int_0^t d\epsilon_v$, $d\epsilon_v = \sqrt{(2/3)d\epsilon_{ij}d\epsilon_{ij}}$, where $d\epsilon_{ij}$ is the incremental plastic strain tensor. The effective strain also achieves a maximum at the same location below the surface.

As the load increases during the impulsive loading, the compressive stress below the surface may reach the material yield point (Fig. 11). From there on, plastic deformations continues to increase until the maximum load is reached. If the load continues to rise beyond that point, an increasing volume of the material undergoes plastic deformation. Later on, as the load amplitude decreases, unloading occurs over a stress-strain line parallel to the initial elastic line, and a permanent indentation or “pit” remains once the load is fully relieved. Fig. 12 shows the effective stress

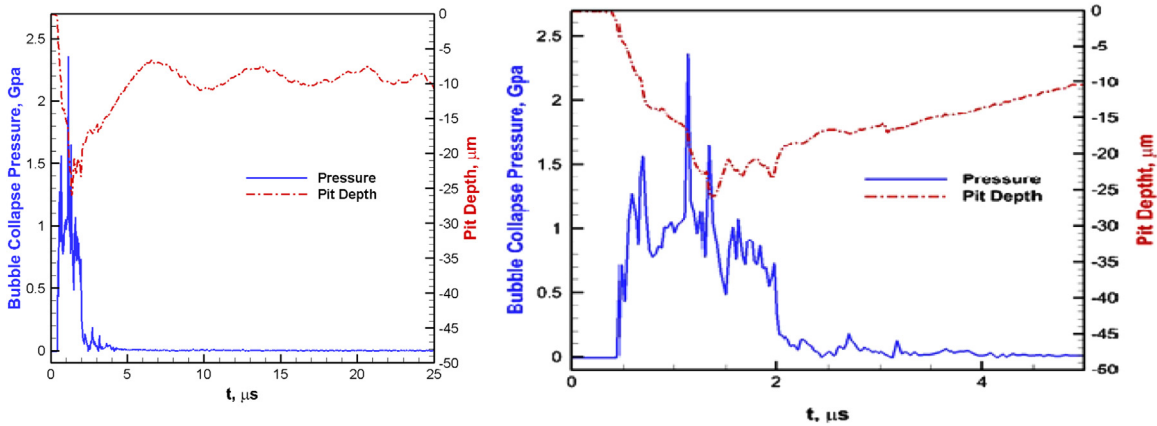


Fig. 10. Time history of pressure and vertical displacement of Al 7075 following the collapse of a cavitation bubble [8] (left), and a zoom between 0 μs and 5 μs (right).

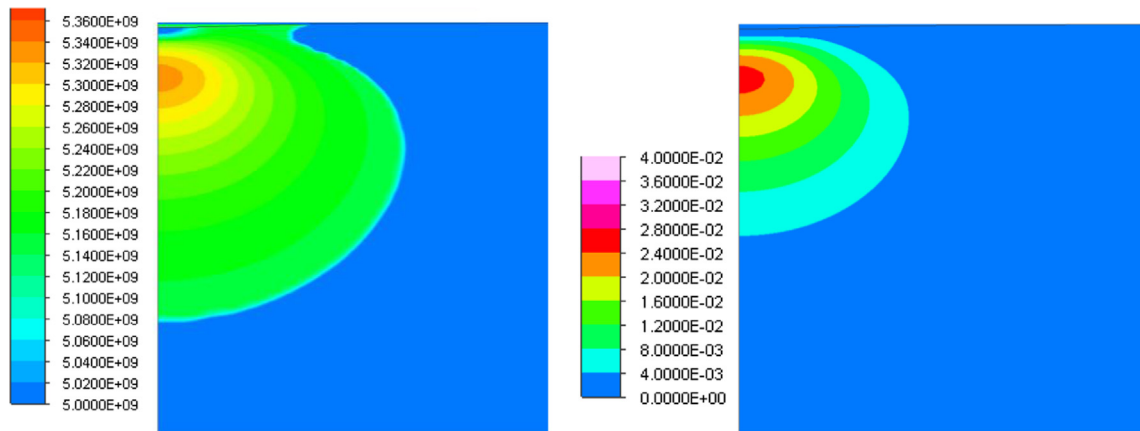


Fig. 11. Effective stress (left) and effective plastic strain (right) at 2.5 μs . Synthetic loading function with duration $\Delta t = 0.1 \mu\text{s}$, spatial radial extent $\Delta r = 100 \mu\text{m}$, and amplitude $P_0 = 2 \text{ GPa}$ on Stainless Steel A2205.

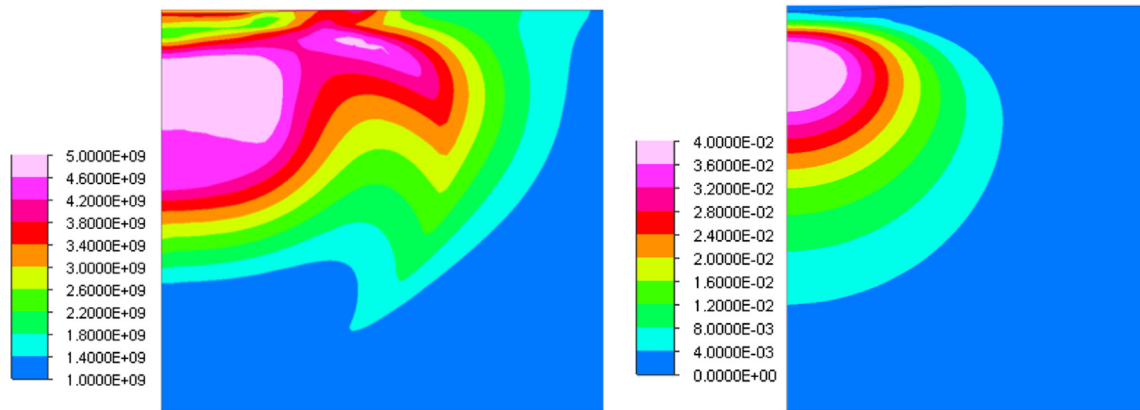


Fig. 12. Effective stress (left) and effective plastic strain (right) at 10 μs . Synthetic loading function with duration $\Delta t = 0.1 \mu\text{s}$, spatial radial extent $\Delta r = 100 \mu\text{m}$, and amplitude $P_0 = 2 \text{ GPa}$ on Stainless Steel A2205.

(left) and effective strain (right) at the end of the computation ($t = 10 \mu\text{s}$) where the permanent deformation has been practically reached. The stress contours show a complex distribution of the residual stresses in the material due to the superposition of stress waves moving away from the center and other incoming waves, which have reflected from the bottom of the material thickness. The strains remaining in the permanently deformed material have a maximum located near the maximum residual stress location. By the time the permanent deformation is reached, the location of the maximum residual stress and strain has moved deeper into the

material, to about twice the depth of the maximum stress and strain locations at the maximum deformation. This change with time of the location of the maximum stresses is also in variance with the Tabor loading determination approach and with other computations assuming constant loading of the material.

5.1.2. Pit depth and diameter

Examples of the permanent deformation predicted from FSI simulations are shown in Fig. 13 through Fig. 15 for both bubble collapse and synthetic loading cases. The profile of the permanent

deformation generated on the surface resembles the experimentally observed pit shapes [1,26] but are significantly different from the spherical shape assumed in the Tabor approach. The three figures also show the Tabor circle corresponding to the spherical shape assumed with the spherical indentation assumptions. In the case of a bubble generated pit, the shape is closer to a cone than a spherical sector. In addition, the pit shape varies significantly, for the same pressure driving bubble collapse conditions, with the standoff distance between the bubble and the wall as illustrated in Fig. 15.

5.2. Strain from pit shape by Tabor formula

Permanent pit shapes obtained from many simulations using both synthetic loading of various pressure peak magnitudes, durations, and radial extents and FSI simulations with various bubble sizes and standoff distances, were computed and analyzed. For all cases, the pit depth was determined from the maximum vertical displacement of the center point on the surface where the maximum deformation occurred. The determination of the pit diameter was based on a method similar to that conventionally used in pit experiments [16,26], i.e. as the diameter of the region where the deformation depth exceeded a set depth criterion. For the numerical computations, a limit value of the deformation of 1 μm, which is of the same order as the height of the material grids near the material surface was selected. (Note that, obviously, any pits with a depth smaller than 1 μm depth are screened out by such a criterion and actually by the numerical simulations itself when the grid size of the order or 1 μm). The cutoff criterion was used to avoid influence of tiny ripples on the surface from numerical simulations oscillations (similarly, from preexisting

surface roughness in the case of experiments). The effect of this criterion on the results was measured and is actually minimal as seen in Table 2. Using the pit geometry in Fig. 14, sensitivity to the pit diameter criterion was investigated by varying the cutoff value from 0.5 μm to 3 μm. The resulting maximum strains obtained from the Tabor relations and the corresponding stresses are summarized in Table 2. It is seen that the used cutoff value for the determination of the pit diameter affects the strains between -3.9% and 13.8%. However, the predicted stress value is not affected too much, and the deviations vary only between -0.7% and 2.3%. As we will see below, these variations are orders of magnitudes less than the errors due to the method itself. (Fig. 15).

Fig. 16 gathers the results of all simulations in one plot and shows pit depths as functions of the magnitude of the peak loads applied to the material. The data covers a large range of loads and pits with the pit depth varying between a few microns and 50 μm. There is obviously a general trend of deeper pits as the peak load increases. However, there is wide scattering in the data with the variation in the loading conditions (i.e. different cavitation bubble history, size of the bubble, duration of the load, etc.). We should also highlight that, as expected, peak loads smaller than a critical load, which is material dependent, do not produce any pits. For such relatively low magnitude loads, the material deforms elastically and then recovers to its original shape once the load is removed, thus leaving no permanent deformation and no formation of a pit. This critical load level depends on the material, and it is of the order of the yield strength of the material.

Fig. 17 shows the pit diameters versus the pressure peak load magnitude for the same computations. Again, there is wide scatter as the pit diameter is not a function of only the magnitude of the load. For small loads which generate local stress lower than the yield stress of the materials, there are no pits. Such data points were excluded from this plot.

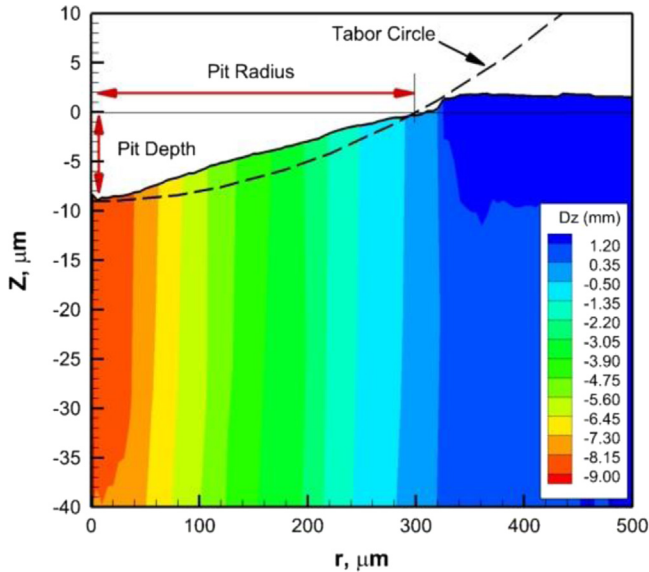


Fig. 13. Profile of the permanent deformation on an Al 7075 plate surface following the collapse of a cavitation bubble. $R_0=50 \mu\text{m}$, $R_{max}=2.0 \text{ mm}$, $P_d=10 \text{ MPa}$, and $\bar{X}=0.75$.

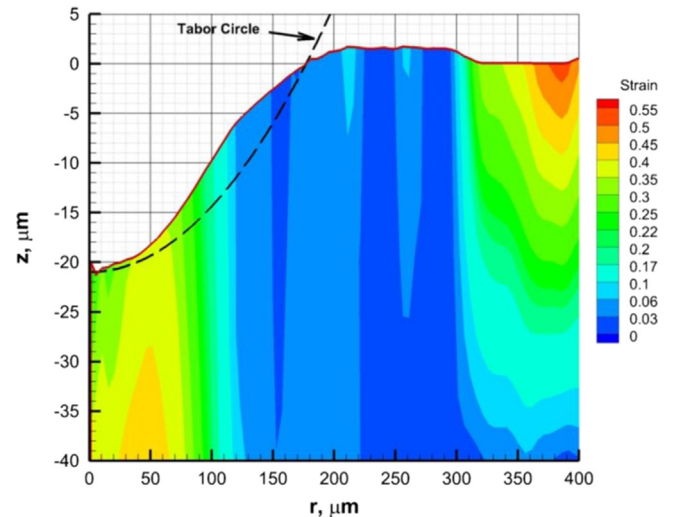


Fig. 14. Predicted pit shape and circular shape used for Tabor formula. Synthetic loading $P_0=5 \text{ GPa}$, $\Delta r=100 \mu\text{m}$, $\Delta t=0.1 \mu\text{s}$ on Al 7075.

Table 2

Sensitivity of the depth threshold in determining the pit diameter and the stress prediction by Tabor formula. The numerically obtained pit geometry in Fig. 14 was used for this analysis.

Cutoff to determine pit diameter (μm)	D (μm)	h (μm)	h/D	ε (Tabor)	% ε deviation from 1 μm case	σ (MPa)	% σ deviation from 1 μm case
0.5	346	21	0.0607	0.146	-3.9%	596	-0.7%
1.0	332	21	0.0633	0.152	0%	600	0%
2.0	312	21	0.0673	0.162	6.2%	607	1.2%
3.0	292	21	0.0719	0.173	13.8%	614	2.3%

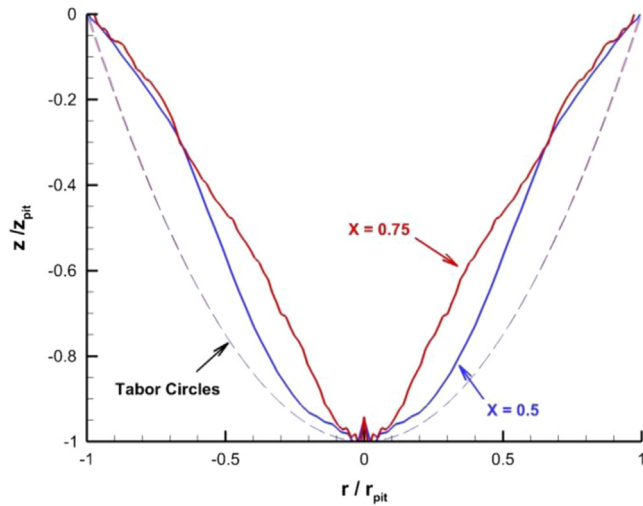


Fig. 15. Comparison of pit shapes between $\bar{X} = 0.5$ and $\bar{X} = 0.75$ for Al7075. $R_0 = 50 \mu\text{m}$, $R_{max} = 2 \text{mm}$, $P_d = 10 \text{MPa}$.

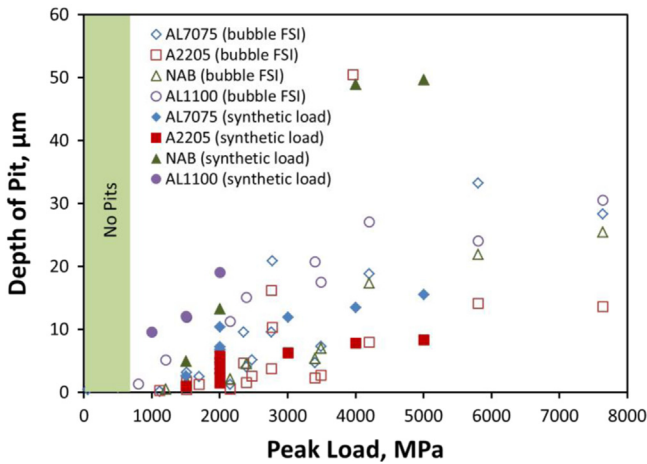


Fig. 16. Pit depth vs. peak pressure for the four materials considered in this study under a set of cavitation bubble dynamics and synthetic loading conditions.

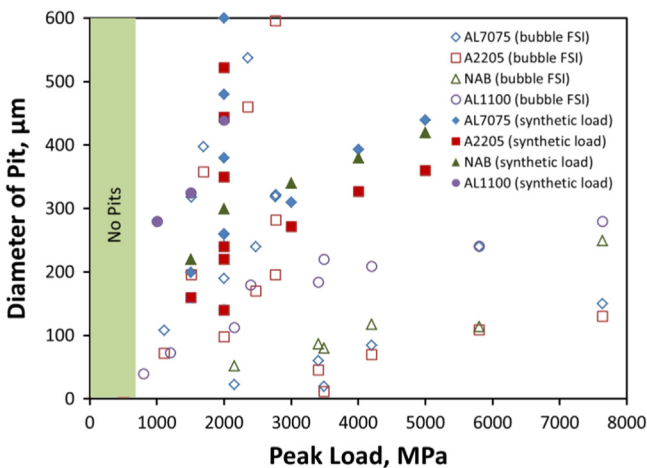


Fig. 17. Pit diameter vs. peak pressure for the four materials considered in this study under a set of cavitation bubble dynamics and synthetic loading conditions.

According to the Tabor's formula, (4), the ratio ξ of pit depth to pit diameter should be related directly to the peak load. To examine this, ξ is plotted in Fig. 18 as a function of the pressure peak load. There is some improvement compared to the pit depth alone or the pit diameter alone correlations, but the scatter is still

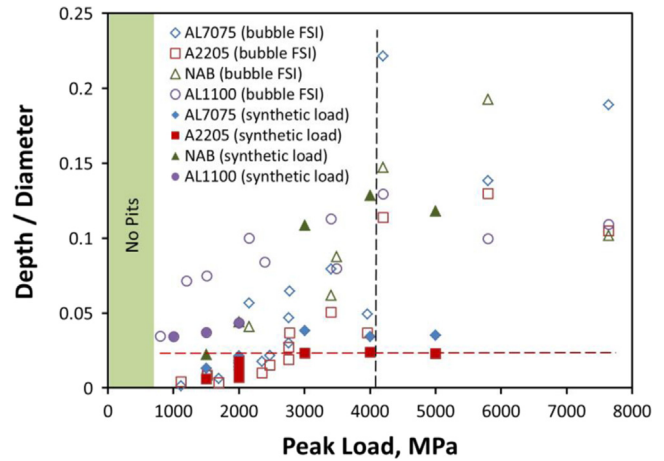


Fig. 18. Pit depth to diameter ratio vs. peak pressure for all materials studied.

extremely large placing in strong doubt for cavitation loading the use of ξ as an index to determine the impact load magnitude.

Fig. 18 collects as a function of the peak load imposed onto the materials the pit depth to diameter ratio, $\xi = h/D$, which according to Tabor's formula determines the load input. The figure clearly shows that the same impulsive pressure obtained from different bubble collapse conditions can produce very different values of ξ , which can vary by an order of magnitude (see for example the data points along the vertical dashed line in the figure). Similarly (see the red dashed horizontal line in the figure) loads which also varied by a factor of more than four produced the same value of ξ . Actually, for a cavitation event, for the same impulsive pressure peak level, the shape of the pressure function can vary significantly, both in space and time, for different bubble sizes, standoffs, and collapse driving pressure functions. In addition, for large strains, strain and stress distributions in the material under the pit deviate significantly from the simple relationship in Eq. (4).

These significant deviations from a one-to-one relationship between the h/D ratio and the imposed peak load are due to a combination of the following over-simplifying assumptions in the Tabor approach and in previous numerical work: spherical indentation, punctual or Gaussian pressure distribution, static load, and absence of interaction between the load and the material. Even for the simple Gaussian distribution, the radial extent of the load, Δr , and the load duration, Δt , have significant effects on the resulting deformation. We have investigated such effects in [33]. For instance, concerning the dynamic effect, the effect of the time duration of the synthetic load on the pits, while keeping all other variables the same, were presented in Fig. 13 of [33] for Al 7075 and SS A2205. Pit diameter was not affected by changing Δt , however the depth to diameter ratios, h/D , changed significantly with Δt . Fig. 19 presents this variation as a percentage deviation from the h/D value at $\Delta t = 2.0 \mu\text{s}$. As can be observed, the depth to diameter ratio depends on the duration of the loading and can be up to 45% higher than the slow loading case.

This demonstrates that conclusions based on a single type of simplified synthetic loading ignoring time dependency and declaring one-to-one correspondence between load and deformation as in [31] are misleading and erroneous.

5.3. Analysis of maximum stress from Tabor relation

To further analyze the above results and understand the reasons for the discrepancy, the mean strain around the pit was deduced from the Tabor relationship (4) and the ratio, ξ , between the pit depth and pit diameter, for all data shown in Fig. 18. The mean strain thus obtained can be related to the maximum strain

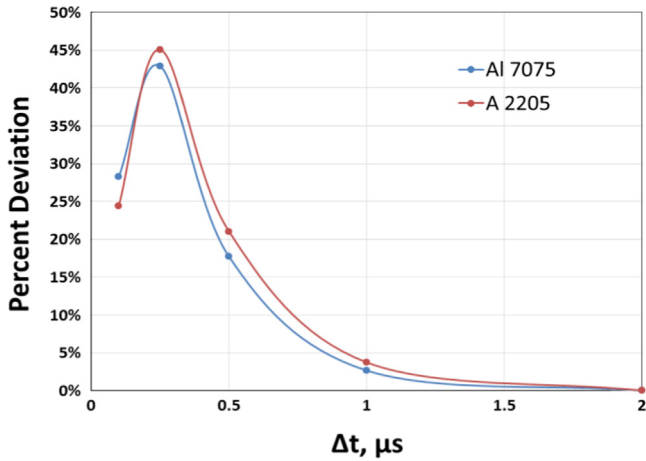


Fig. 19. Percent deviation of pit depth to diameter ratio relative to the value at $\Delta t=2 \mu s$ vs. peak pressure duration for aluminum Al 7075 and stainless steel A2205.

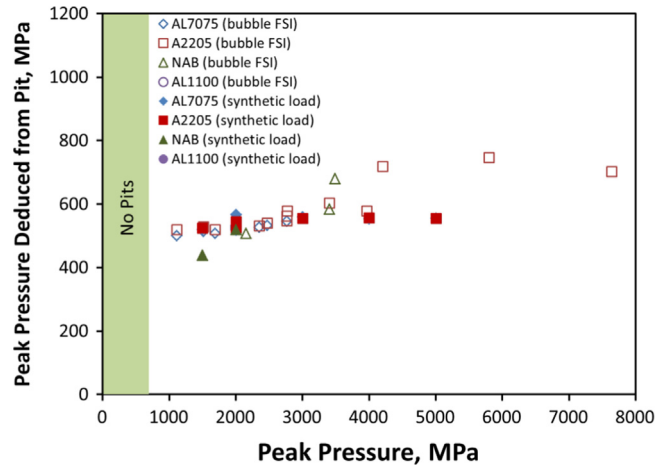


Fig. 21. Stress predicted from Tabor formula using the computed pit depth to diameter ratios under the various loading condition of the four materials.

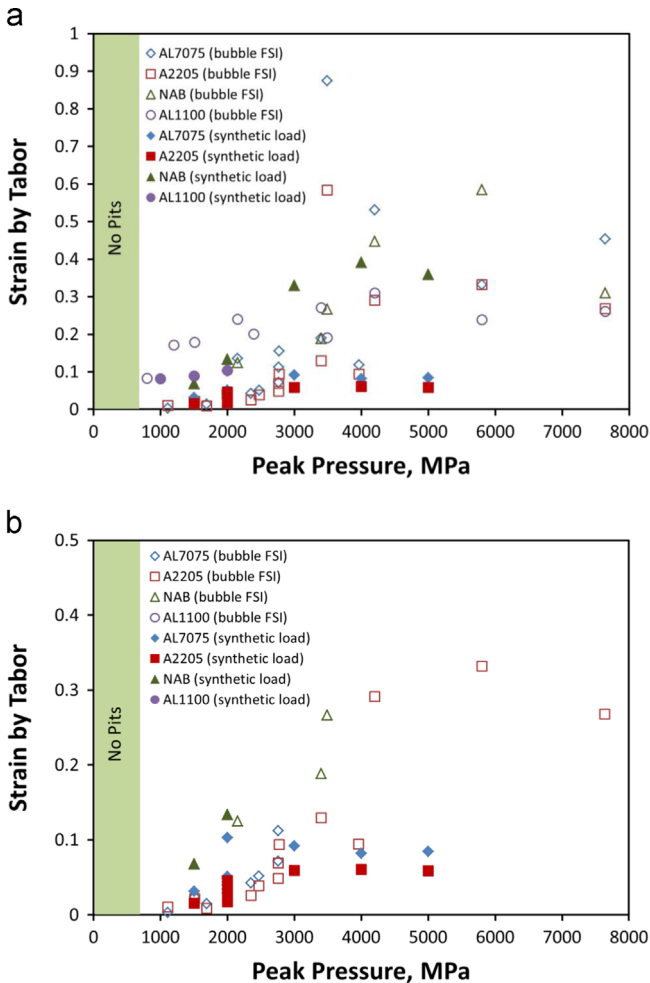


Fig. 20. Maximum strains predicted from the Tabor formula using the computed pit depth to diameter ratios under the various loading condition of the four materials: (a) all data points with some exceeding ultimate strain included, (b) only data points below ultimate strain.

based on the assumption of Eq. (5), i.e. exponential distribution of strain in the depth direction. The θ values reported in [46] were used here. These values are 2.0 for Al 7075, 2.8 for NAB and 2.2 for SS A2205. The value for Al 1100 is unknown, and we used the same

value as for Al 7075 (2.0). One should therefore ignore the data for Al100 if this value may be too far from reality.

The $\xi = h/D$ ratios were converted to maximum strains using Eq. (5) as shown in Fig. 20. This provides maximum strains in the 10% to 20% range for peak loads up to 2 GPa. Larger strains exceeding 30% were found for peak loads larger than 3 GPa. As the strain becomes larger, the distribution of the strains and stresses in the material around the pit deviate from a simple proportional relationship in the Tabor relationship and this contributes to the even larger scatter at higher loading. Fig. 20a shows all data, including those where the strains exceeded the ultimate strains and where the computations are no longer valid. Fig. 20b shows only valid data where conditions where strains exceeding the ultimate strains have been excluded.

Using the stress–strain curves in Fig. 2, maximum stresses were deduced from the maximum strains and this is shown in Fig. 21 as a function of the loading pressure peak magnitudes. This brings the data closer to a common curve by accounting for differences in the materials properties. However, wide scatter remains for well-defined pits and there is inability to differentiate small loads (below about 1 GPa), which did not produce well defined pits. The figure also shows that the values of the maximum stresses predicted from the pit geometries deviate very significantly from the corresponding applied pressure loads. While the peak loads varied from 1 GPa to 8 GPa, the predicted maximum stresses were much lower varying between 500 MPa and 1 GPa. This discrepancy comes from the difference between the applied maximum load at the surface and the maximum effective stress observed in the material which is more directly related to the amount of deformation and thus the pit depth. This is discussed further below.

A comparison for each data loading condition between the maximum stress and the peak value of the impulsive pressure applied to the material is shown in Fig. 22. This comparison highlights that for all data, the maximum stress predicted from the pit is much lower than the actual applied load (good correspondence would be the purple line in the plot). In this representation, the slope of the pit based prediction is of the order of 20 while it should have a value of 1 for an accurate prediction.

5.4. Comparison of pressure imposed, pressure deduced, and maximum effective stress

We discussed above the differences between the actual imposed pressure peaks and those deduced from the pit geometry and Tabor relations. Here we consider the maximum von-Mises (or maximum equivalent) stresses seen by the material. In this study,

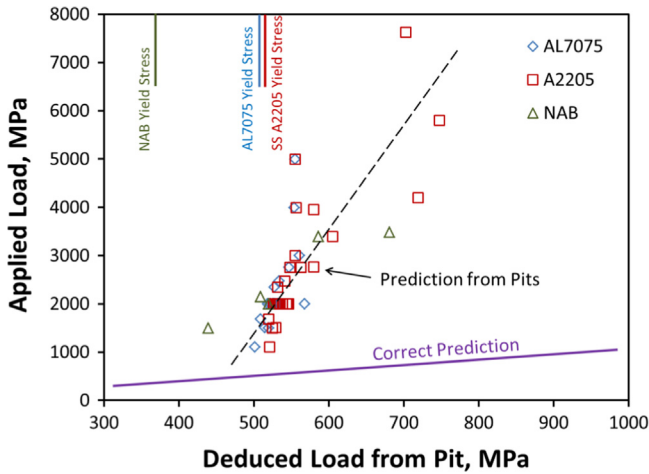


Fig. 22. Comparison of the peak pressure applied to the material deduced from Tabor pit analysis with the actual applied pressure.

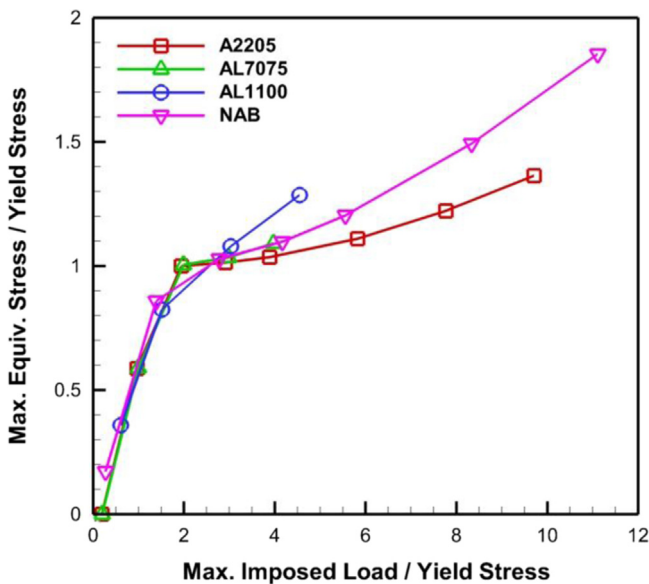


Fig. 23. Maximum effective stress recorded in the material during the whole duration of simulation plotted against the maximum amplitude of the imposed load. Both the axes are normalized by the yield strength of respective materials. Synthetic loading with $\Delta t=0.1 \mu s$, $\Delta r=100 \mu m$.

the maximum effective stress experienced by the material was extracted directly from the FEM simulations of the material dynamics for each of the simulations presented above. This maximum was obtained by scanning through each FEM solution both in time and in space. Fig. 23 shows, for all four materials, the maximum effective stresses recorded in the material normalized by the yield stress of each material as functions of the applied pressure also normalized by the yield stress of each material. For clarity of the representation, only synthetic computations are shown but the results apply to all data. We can see that for small imposed loads, the maximum effective stress increases linearly with the peak load. However, once the maximum effective stress exceeds the yield stress of the material, the slope of the curve decreases due to the material experiencing permanent deformation in the plastic regime. With increased load, the slope in the plastic regime curves increases again. As expected with this representation, the linear part of the curve below the yield stress is common to different materials, but the plastic part above the yield stress is dependent on the material.

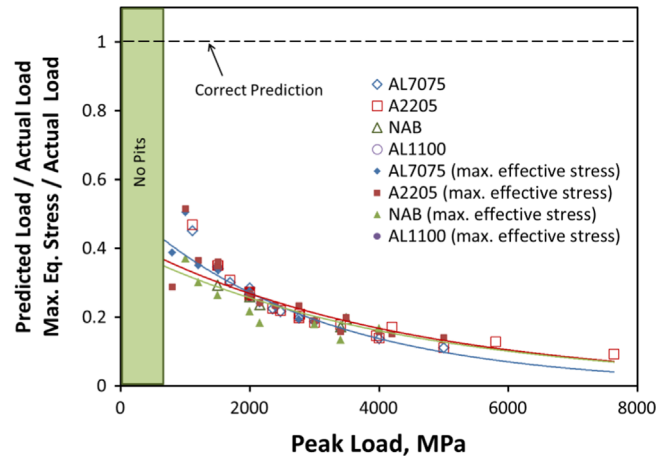


Fig. 24. Ratio of predicted peak load to actually imposed peak load and comparison with the ratio of maximum effective stress to imposed peak load versus peak load.

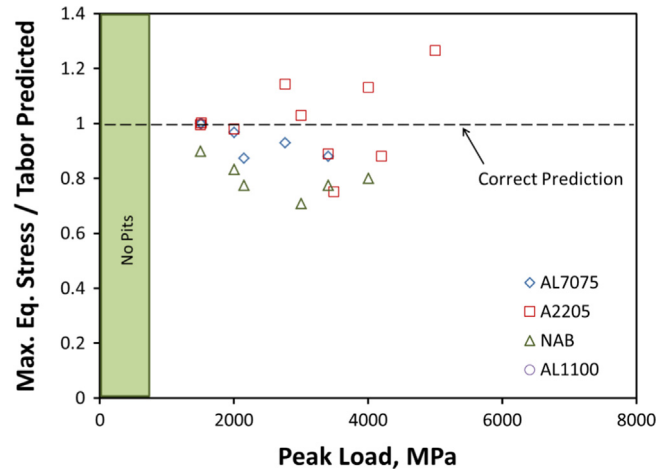


Fig. 25. Ratio of maximum effective stress to Tabor-pit geometry deduced stress versus peak load.

The ratio of the pressures predicted from the pit geometrical shape ratio ξ and the Tabor relation to the actually applied pressure peak is plotted in Fig. 24. The data from the Tabor relation forms, for all materials, roughly a curved band significantly lower than 1. The actual pressure divided by the pit-Tabor predicted pressure significantly increases with increasing loads exceeding 10 at the highest load values. Fig. 24 also shows the numerically computed maximum effective stress inside the material for comparison. It is evident that the stress deduced from the Tabor relation agrees well with this maximum effective stress (von Mises stress) recorded in the material (not at the surface) and not the imposed load! The maximum effective stress is only 10% to 60% of the peak load depending on the magnitude of the load, which explains the above described discrepancies. Fig. 25 further shows the level of accuracy of the Tabor-pit prediction of the maximum von-Mises stresses inside the material (not at the surface). The ratio is not actually one but it is much closer to one (by an order of magnitude – compare with Fig. 24) than the ratio of predicted load to applied load.

6. Conclusions

In this paper, the development of permanent deformation pits on a metallic material surface due to cavitation pressure loading was studied using fluid/material interaction numerical simulations.

The study aimed at establishing a relationship between the impact pressure load and the resulting pit size, which would be a suitable input to the inverse problem of predicting pressure peaks from pitting tests and resulting pit size statistics. The analytic relation based on Tabor's formula appears to not be able to provide this load correctly and underestimates it by a large factor. Instead, Tabor's relation provides quite accurately the maximum effective stress experienced by the material and this applies for all four metals used in this study. This study strongly suggests that the correlation of pitting tests with the pressure field of an erosive cavitation field intensity is at best qualitative and that the material itself cannot be used with pitting and the Tabor formula as a sensor of the fluid generated pressures.

Acknowledgments

This work was conducted under support from DYNFLOW, Inc. internal IR&D 2015-02 and partial support from the Office of Naval Research under Contract N00014-12-M-0238, monitored by Dr. Ki-Han Kim. We would like to thank Dr. Kim for his support. We are also grateful to many colleagues at DYNFLOW, who have contributed to several aspects of this study, most particularly, Dr. Chao-Tsung Hsiao and Dr. Anil Kapahi for their contributions.

References

- [1] K.-H. Kim, G.L. Chahine, J.-P. Franc, A. Karimi, *Advanced Experimental and Numerical Techniques for Cavitation Erosion Prediction*, Series Fluid Mechanics and Its Applications, Springer, Berlin, Germany, 2014.
- [2] R.T. Knapp, J.W. Daily, F.G. Hammit, *Cavitation*, McGraw-Hill, London, 1970.
- [3] F.G. Hammit, *Cavitation and Multiphases Flow Phenomena*, McGraw-Hill, New York, 1980.
- [4] C.E.E. Brennen, *Cavitation and Bubble Dynamics*, Oxford University Press, New York, 1995.
- [5] J.R. Blake, B.B. Taib, G. Doherty, *Transient cavities near boundaries. Part 1. Rigid boundary*, *J. Fluid Mech.* 170 (1986) 479–497.
- [6] S. Zhang, J. Duncan, G.L. Chahine, *The final stage of the collapse of a cavitation bubble near a rigid wall*, *J. Fluid Mech.* 257 (1993) 147–181.
- [7] G.L. Chahine, *Modeling of cavitation dynamics and interaction with material*, in: A. Kim, K.-H. Chahine, G.L. Franc, J.-P. Karimi (Eds.), *Advanced Experimental and Numerical Techniques for Cavitation Erosion Prediction*, Springer, Berlin, 2014, pp. 123–173.
- [8] C.-T. Hsiao, A. Jayaprakash, A. Kapahi, J.-K. Choi, G.L. Chahine, *Modelling of material pitting from cavitation bubble collapse*, *J. Fluid Mech.* 755 (2014) 142–175.
- [9] G.L. Chahine, C.-T. Hsiao, *Modeling cavitation erosion via bubble-material interaction*, *Interface Focus* 5 (5) (2015).
- [10] P.A. Lush, *Impact of a liquid mass on a perfectly plastic solid*, *J. Fluid Mech.* 135 (1983) 373–387.
- [11] H. Soyama, D.O. Macodiyo, S. Mall, *Compressive residual stress into titanium alloy using cavitation shotless peening method*, *Tribol. Lett.* 17 (3) (2004) 501–504.
- [12] G.L. Chahine, C.-T. Hsiao, A. Kapahi, J.-K. Choi, *Coupling bubble and material dynamics to model cavitation peening and pitting*, in: *ICFD-2015*, 2015.
- [13] S. Singh, J.-K. Choi, G.L. Chahine, *Characterization of cavitation fields from measured pressure signals of cavitating jets and ultrasonic horns*, *J. Fluids Eng.* 135 (9) (2013) 9111–91302.
- [14] A. Thiruvengadam, *Handbook of cavitation erosion*, *Hydraulics Tech. Rep.* (no. 7301-1), 1974.
- [15] P. Eisenberg, H.S. Preiser, A. Thiruvengadam, *On the mechanisms of cavitation damage and methods of protection*, *Trans. Soc. Nav. Archit. Mar. Eng.* 73 (1965) 241–286.
- [16] J.-P. Franc, G.L. Chahine, A. Karimi, *Pitting and incubation period*, in: K.-H. Kim, G.L. Chahine, J.-P. Franc, A. Karimi (Eds.), *Advanced Experimental and Numerical Techniques for Cavitation Erosion Prediction*, 160, Springer, Berlin, 2014, pp. 37–70.
- [17] C.A. Parsons, S.S. Cook, *Investigation into causes of corrosion or erosion of propellers*, *J. Am. Soc. Nav. Eng.* 31 (1919) 536–541.
- [18] R.T. Knapp, *Recent investigations of the mechanics of cavitation and cavitation damage*, *Trans. Am. Soc. Mech. Eng.* 77 (1955) 1045–1054.
- [19] R.T. Knapp, *Accelerated field tests of cavitation intensity*, *Trans. Am. Soc. Mech. Eng.* 80 (1958) 91–102.
- [20] J.M. Dorey, E. Laperrousaz, P. Avellan, P. Dupont, R. Simoneau, P. Bourdon, *Cavitation erosion prediction on Francis turbines – Part 3 methodologies of prediction*, in: *Proceedings of the XVIII IAHR Symposium on Hydraulic Machinery and Cavitation*, 1996.
- [21] N. Berchiche, J.-P. Franc, J.M. Michel, *A cavitation erosion model for ductile materials*, in: *Proceedings of the 4th International Symposium on Cavitation*, CAV2001, 2001.
- [22] M. Farhat, P. Bourdon, P. Lavigne, R. Simoneau, *The Hydrodynamic aggressiveness of cavitating flows in hydro turbines*, in: *Proceedings of Fluids Engineering Division Summer Meeting, FEDSM'97*, 1997.
- [23] M.L. Billet, *The specialist committee on cavitation erosion on propellers and appendages on high powered/high speed ships. Final report and recommendations to the 24th ITTC*, in: *Proceedings of the 24th International Towing Tank Conference*, vol. II, 2005.
- [24] D.R. Stinebring, J.W. Holl, R.E.A. Arndt, *Two aspects of cavitation damage in the incubation zone: Scaling by energy considerations and leading edge damage*, *J. Fluids Eng.* 102 (1980) 481–485.
- [25] M. Dular, B. Stoffel, B. Sirok, *Development of a cavitation erosion model*, *Wear* v261 (2006) 642–655.
- [26] A. Jayaprakash, J.-K. Choi, G.L. Chahine, F. Martin, M. Donnelly, J.-P. Franc, A. Karimi, *Scaling study of cavitation pitting from cavitating jets and ultrasonic horns*, *Wear* 296 (1–2) (2012) 619–629.
- [27] A. Karimi, J.-P. Franc, *Modeling of material response*, in: K.-H. Kim, G. Chahine, J.-P. Franc, A. Karimi (Eds.), *Advanced Experimental and Numerical Techniques for Cavitation Erosion Prediction*, Springer, Berlin, Germany, 2014, pp. 163–180.
- [28] D. Carnelli, A. Karimi, J.-P. Franc, *Evaluation of the hydrodynamic pressure of cavitation impacts from stress-strain analysis and geometry of individual pits*, *Wear* 289 (2012) 104–110.
- [29] D. Tabor, *The Hardness of Metals*, Clarendon Press, Oxford, United Kingdom, 1951.
- [30] F. Pöhl, S. Mottlyll, R. Skoda, S. Huth, *Evaluation of cavitation-induced pressure loads applied to material surfaces by finite-element-assisted pit analysis and numerical investigation of the elasto-plastic deformation of metallic materials*, *Wear* (2015).
- [31] S.C. Roy, J.-P. Franc, C. Pellone, M. Fivel, *Determination of cavitation load spectra – Part 1: static finite element approach*, *Wear* (2015).
- [32] S.C. Roy, J.-P. Franc, N. Ranc, M. Fivel, *Determination of cavitation load spectra – Part 2: dynamic finite element approach*, *Wear* (2015).
- [33] J.-K. Choi, A. Jayaprakash, A. Kapahi, C.-T. Hsiao, G.L. Chahine, *Relationship between space and time characteristics of cavitation impact pressures and resulting pits in materials*, *J. Mater. Sci.* 49 (8) (2014) 3034–3051.
- [34] K.M. Kalumuck, R. Duraiswami, G.L. Chahine, *Bubble dynamics fluid-structure interaction simulation by coupling fluid BEM and structural BEM codes*, *J. Fluids Struct.* 9 (8) (1995) 861–883.
- [35] G.L. Chahine, R. Duraiswami, K.M. Kalumuck, *Boundary element method for calculating 2-D and 3-D underwater explosion bubble behavior in free water and near structures*, *Nav. Surf. Warf. Center Weapons Res. Technol. Dep. no., Report NSWCDD/TR-93/46*, 1996.
- [36] A. Wardlaw, J.A. Luton, *The Gemini Euler solver for the coupled simulation of underwater explosions*, *NSWCIH – Tech. Rep. (no. 2500)*, 2003.
- [37] C.-T. Hsiao, G.L. Chahine, *Development of compressible-incompressible link to efficiently model bubble dynamics near floating body*, in: *Advances in Boundary Element Meshless Techniques XIV*, 2013.
- [38] K.M. Kalumuck, G.L. Chahine, C.-T. Hsiao, *Simulation of surface piercing body couples response to underwater bubble dynamics utilizing 3DynaFS(c), a three-dimensional BEM code*, *Comput. Mech.* 32 (4–6) (2003) 319–326.
- [39] A. Kapahi, C.-T. Hsiao, G.L. Chahine, *A multi-material flow solver for high speed compressible flow applications*, *Comput. Fluids* (2015), <http://dx.doi.org/10.1016/j.compfluid.2015.03.016>.
- [40] G.L. Chahine, R. Annasami, C.-T. Hsiao, *Scaling of the re-entering jet parameters of an underwater explosion bubble below a floating structure*, in: *Proceedings of the 74th Shock and Vibration Symposium*, 2002.
- [41] A.B. Wardlaw, J.A. Luton, *Fluid-structure interaction mechanisms for close-in explosions*, *Shock Vib.* 7 (2000) 265–275.
- [42] J.I. Lin, *DYNA3D: a nonlinear, explicit, three-dimensional finite element code for solid and structural mechanics*. User manual, *Laurence Livermore Natl. Lab.*, no. UCRL-MA-107254, 2005.
- [43] A. Jayaprakash, G.L. Chahine, C.-T. Hsiao, *Numerical and experimental study of the interaction of a spark-generated bubble and a vertical wall*, *ASME J. Fluids Eng.* 134 (3) (2012) 31301–31312.
- [44] G.R. Johnson, W.H. Cook, *A constitutive model and data for metals subjected to large strains, high strain rates and high temperatures*, in: *Proceedings of the 7th International Symposium on Ballistics*, 1983, pp. 541–547.
- [45] G.L. Chahine, Y. Shen, *Bubble dynamics and cavitation inception in cavitation susceptibility meters*, *ASME J. Fluids Eng.* 108 (4) (1986) 444–453.
- [46] G.L. Chahine, J.-P. Franc, A. Karimi, *Part 1: cavitation and cavitation erosion – computational and experimental approaches*, in: K.-H. Kim, G.L. Chahine, J.-P. Franc, A. Karimi (Eds.), *Advanced Experimental and Numerical Techniques for Cavitation Erosion Prediction*, Springer, Berlin, 2014.